CrossMark

ARTICLE

Toward a better understanding of conjugated polymer blends with non-spherical small molecules: coupling of molecular structure to polymer chain microstructure

Michael Roders, Vincent V. Duong, and Alexander L. Ayzner[a)]
Department of Chemistry and Biochemistry, University of California, Santa Cruz, Santa Cruz, CA 95064, USA

(Received 1 October 2016; accepted 23 November 2016)

A major obstacle in the organic solar cell field is the inability to predict the relevant microstructural length scales that determine charge transport of the interpenetrating polymer/small molecule network based on the component chemical structures. This has led to a trial-and-error approach, which is extremely labor-intensive. This manuscript is our attempt to move toward forming a link between small molecule chemical structure and the morphological hierarchy of the blend. We focus on geometric motifs of small molecule organic semiconductors which have 2D, nonspherical 3D, and quasispherical 3D molecular orbital extent. We find that phase separation in these blends is a function of the molecular structure, and that the small molecule chemical structure is coupled to the crystallite orientation distribution of the polymer matrix. We further find that the ability of a molecule to form a network with a well-defined length scale of phase separation depends on the polymer persistence length.

I. INTRODUCTION

The organic photovoltaic (OPV) field has matured substantially since the initial discovery of ultrafast photoinduced electron transfer from a conjugated polymer to a fullerene derivative in a thin blend film.[1] After the quick realization that efficient OPV devices must incorporate a large density of electron donor/acceptor interfaces, the bulk heterojunction architecture (BHJ) was born.[2] Though various combinations of conjugated polymer and small molecule devices have been explored to date, conjugated polymer/fullerene derivative blends have by far received the most attention, primarily due to their facile thin film processing.[3–5] In OPV devices, photogenerated electronic excited states (excitons) spatially diffuse until they relax to the ground state or encounter a donor/acceptor interface, where electron–hole pair disassociation occurs, leading to holes localized on the donor(s) and electrons on the acceptor(s). If the spatially separated electron and hole can overcome their binding energy, both charges migrate away from the heterointerface, driven by a combination of electric and chemical potential gradients.[6–8]

It is a remarkable fact that a straight-forward means of creating a relatively efficient OPV device is by simply letting the solvent evaporate from a thin liquid layer of solution comprised of the donor/acceptor blend. The nonequilibrium thermodynamics of solvent evaporation along with the hydrodynamic forces acting on the solution during thin film formation determine the initial state of the blend film. The resulting solid film contains an interpenetrating donor/acceptor network, whose mean length scale of phase separation is known to be a function of various processing variables, such as choice of solvent, thermal and solvent annealing, solvent additives, etc.[4,9–13] As the extent of donor/acceptor phase separation varies, the volume spanned by charge-transporting paths changes for both charges, thus changing the tortuosity of charge flow.

The extent of phase separation and intermixing between donor and acceptor molecules within the BHJ film has a limiting effect on the relative rates of electron–hole separation and the formation of percolated donor-rich and acceptor-rich paths that allow charges to reach the electrodes. A fundamental requirement is that the mean length scale of donor/acceptor segregation be commensurate with the exciton diffusion length—the distance that excitons traverse during their lifetime. The exciton diffusion length of typical organic semiconductors is of order 10 nm.[14–19] Thus, the relevant morphological length scales lie in the 10 s of nanometers range. Very fine mixing between donor and acceptor molecules result in large charge generation yields but low photocurrents due to poor charge mobilities and large recombination rates. A highly segregated network yields few charges due to the relatively low donor/acceptor interfacial area, but the charge mobility rises substantially owing to a less tortuous morphology and decreased bimolecular recombination rates. The fine balancing act

Contributing Editor: Moritz Riede
[a)]Address all correspondence to this author.
e-mail: aayzner@ucsc.edu
DOI: 10.1557/jmr.2016.490

 © Materials Research Society 2017

https://doi.org/10.1557/jmr.2016.490 Published online by Cambridge University Press

of finding the "sweet spot" in a highly multidimensional processing variable space corresponding to the optimal blend morphology is a very laborious task that must be painstakingly performed for every new donor/acceptor combination.

The latest progress in the polymer-based OPV field has primarily been achieved via conjugated polymer band gap engineering to increase the spectral overlap of the polymer absorption coefficient with the solar emission spectrum.[20–22] At the same time, the most commonly utilized electron acceptors, the mono-functionalized C_{60} and C_{70} derivatives $PC_{60}BM$ and $PC_{70}BM$, respectively —used with overwhelming frequency—have changed very little. Due to their quasispherical electronic wavefunctions, fullerenes are remarkable electron acceptors that boast nearly isotropic inter-fullerene electron transfer rates—qualities that are paramount to an effective electron transport network.[23,24] However, fullerene derivatives have notably low absorption cross-sections and thus contribute relatively little to the photocurrent, particularly in the near-IR region of the spectrum.[25] Additionally, the reliance on fullerene derivatives as a standard molecular acceptor has potentially limited the breadth of polymer hosts that have been explored, as polymer energy levels must match those of the fullerene.

Improving upon fullerene-based OPV devices with a nonfullerene electron acceptor is an extremely tall order. Though the frontier energy levels can be matched in a straight-forward manner,[26] replicating the highly desirable mesoscale charge mobility of the fullerene network is very challenging. This is primarily because most organic small molecules are anisotropic, which leads to intermolecular electron transfer rates that depend strongly on the relative molecular orientation,[27–29] expectedly leading to certain charge transport directions characterized by very poor charge mobilities. Progress is substantially hampered by a lack of fundamental understanding that connects the chemical structure of the small molecule to the hierarchical, Å- to nanometer-scale microstructure of the BHJ film. The purpose of this manuscript is to begin to systematically make this connection. To do so, we have used a combination of X-ray scattering techniques to interrogate polymer/small molecule blends as a function of small molecule structure and polymer chain microstructure. The small molecule set contains three distinct geometric motifs, which can be roughly characterized as representing 2D, quasispherical 3D, and nonspherical 3D frontier molecular orbital extent. Our results show that, not only is the morphology a sensitive function of the small molecule chemical structure and the polymer chain microstructure, but that the polymer crystallite orientation distribution similarly depends on the small molecule structure. Our results underscore that when designing new electron acceptors, the polymer/small molecule blend must effectively be viewed as a coupled super-molecule, and that the polymer microstructure may dictate the preferred geometric motif of the small molecule.

II. RESULTS

To begin elucidating the influence of both small molecule chemical structure and polymer host chain microstructure on the morphology of thin blend films, we have used synchrotron X-ray scattering to simultaneously characterize the Å- and the nanometer (meso)-scale morphology of the molecular series shown in Fig. 1. Recent work has shown that high crystallinity of the polymer matrix is not a necessary condition for efficient device function, and that largely amorphous polymer can yield substantial power conversion efficiencies.[30] Thus, it is important to understand the behavior of the small molecule in blends that encompass both amorphous and semicrystalline polymer matrices. As such, below we have focused on both the amorphous regiorandom poly (3-hexylthiophene) (raP3HT) and the polycrystalline regioregular P3HT (reP3HT), with the two polymers having very similar molecular weights.

This work is concerned with the influence of molecular shape and molecular orbital dimensionality of the small molecule on the film microstructure; therefore, the small molecule set shown in Fig. 1 comprises several representative dimensionality classes. The methoxyphenyl perylene diimide (PDI) derivative has a planar conjugated core, which contains the bulk of the frontier orbital electron density, and thus represents a quasi-2D molecule with highly anisotropic intermolecular interactions due to π-stacking of the core. The Spiro-MeOTAD derivative, though usually not an acceptor itself based on the relative position of energy levels, is a small molecule with molecular orbitals that do not lie in the same plane due to the bridging sp^3 carbon atom and the peripheral tertiary amines. As such, this is an example of a molecule with a quasi-3D molecular orbital extent. Such a geometry represents a case of a small molecule, whose intermolecular interactions may lead to more isotropic charge transfer rates. Indeed, this general geometry has recently been used as the basis for a new nonfullerene electron acceptor. 3D chemical structures are shown in Fig. S7 of the Supplementary Material. Finally, as the representative of the quintessential 3D quasispherical molecule, phenyl-61-butyric acid methyl ester (PCBM) will be used as the reference point due to its previously explored morphology.

To characterize local order on the Å scale, which strongly influences intermolecular electron transfer rates, we begin by discussing 2D grazing-incidence X-ray diffraction (GIXD) patterns,[31–35] followed by analysis of the polymer crystallite orientation distribution functions. We then move to grazing-incidence (diffuse)

https://doi.org/10.1557/jmr.2016.490 Published online by Cambridge University Press

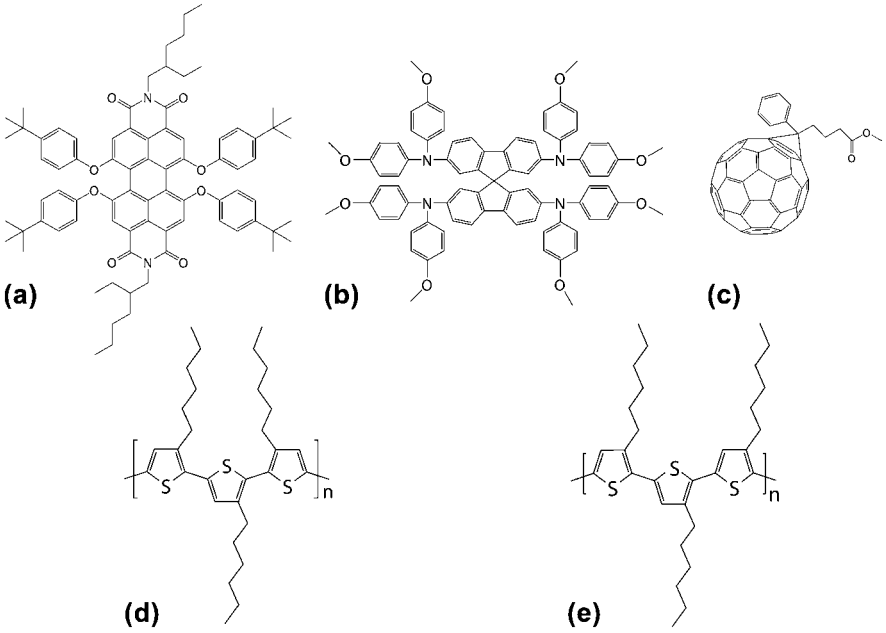


FIG. 1. Chemical structures of the small molecules (a–c) and conjugated polymers used in this investigation. (a) perylene diimide derivative (PDI) with 2D spatial frontier orbital extent; (b) spirobifluorene derivative (Spiro-MeOTAD) with frontier electron density delocalized in 3D due to its equilibrium geometry; (c) mono-functionalized fullerene derivative (PCBM), whose molecular orbitals are delocalized over the quasi-spherical cage. (d) regiorandom P3HT; (e) regioregular P3HT. Regiorandom P3HT contains a distribution of relative monomer orientations, of which only one is captured by the shown structure.

small-angle X-ray scattering (GISAXS) to probe the mesoscale morphology of the blend, which ultimately dictates both the efficiency of exciton dissociation and percolated long-distance charge transport through the interpenetrating polymer/molecule network. To further aid interpretation of the mesoscale morphology, GISAXS measurements are complimented by resonant elastic X-ray scattering (REXS) measurements performed in the vicinity of the carbon K-edge absorption onset.

A. Å-scale microstructure

We start by exploring reP3HT and its blends. As expected, pristine reP3HT forms ordered semicrystalline films illustrated by three orders of (h00) Bragg peaks in the out-of-plane direction, indicative of end-to-end lamellar packing with a spacing of d = 16.5 Å, consistent with previous reports.[11,13,36–38] This is shown in Fig. S1 of the Supplementary Material. Bragg reflections in reP3HT films are angularly dependent, with highest intensity occurring along the Q_z axis, indicating that lamellae are packed predominantly edge-on with respect to the substrate. Consistent with this orientation, the inter-chain backbone π-stacking is primarily in-plane, as evident by a high-intensity (010) reflection near Q_{xy} ~1.67 Å^{-1} with a d-spacing of 3.76 Å.

Figure 2 shows GIXD images for both reP3HT and raP3HT blended with the three small molecules at a fixed monomer/molecule mole ratio corresponding to a 1:1 w/w P3HT:Spiro-MeOTAD blend. All shown films were thermally annealed. Blending reP3HT with PCBM results in the addition of a broad halo centered at Q ~1.35 Å^{-1} due to scattering by amorphous PCBM aggregates. The polycrystalline features of reP3HT are retained with a bimodal lamellar crystallite orientation distribution indicated by the Q = 0.38 Å^{-1} (100) reflection with intensity peaking near the Q_z and Q_{xy} axes. Such a distribution is consistent with the presence of a bimodal (010) Bragg reflection. GIXD images of reP3HT blends with PDI [Fig. 2(b)] follow a qualitatively similar trend compared to PCBM blends, with (h00) reflections with highest intensity along the Q_z and Q_{xy} axes, indicating preferred crystallite orientations in both edge-on and face-on fashions. Blends of reP3HT with Spiro-MeOTAD show a P3HT crystallite orientation distribution that differs qualitatively from both PCBM and PDI. Specifically, the orientation changes to primarily edge-on, similar to neat reP3HT films (Fig. 3).

In contrast to reP3HT, raPHT is amorphous in both neat films and blends, even after thermal annealing. This is due to the fact that, on average, raPHT has a shorter delocalization length of its electronic wavefunction compared to reP3HT, leading to weak inter-chain interactions and thus little propensity to crystallize. Since wavefunction delocalization tends to planarize the polymer backbone, reP3HT is characterized by a larger persistence length than raP3HT. This quantity is related to the mean chromophore size, which is a nontrivial quantity to estimate. The amorphous nature of raP3HT is evident

https://doi.org/10.1557/jmr.2016.490 Published online by Cambridge University Press

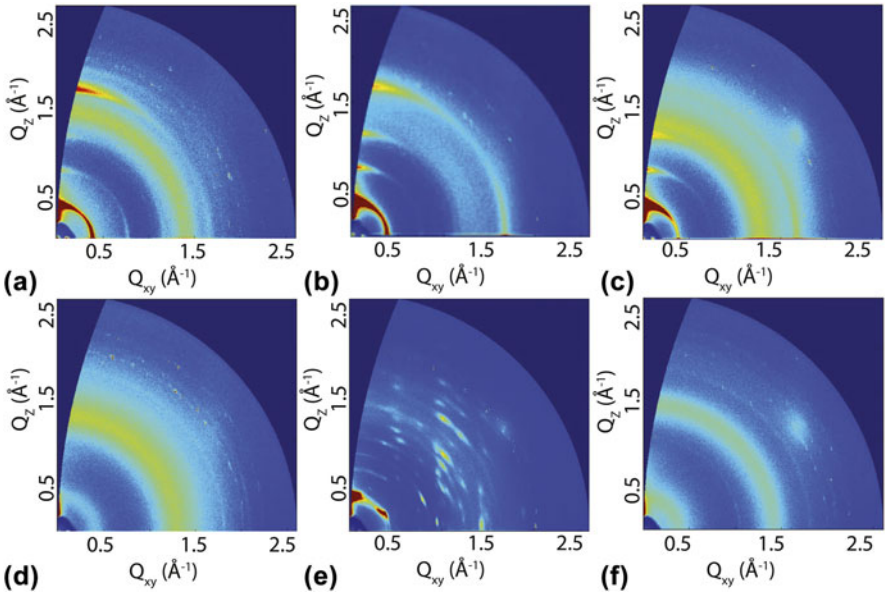


FIG. 2. 2D GIXD patterns of thermally annealed thin film blends of reP3HT with (a) PCBM, (b) PDI, and (c) Spiro-MeOTAD, as well as raP3HT with (d) PCBM, (e) PDI, and (f) Spiro-MeOTAD. reP3HT blends show characteristic (*h00*) lamellar diffraction peaks of the semicrystalline polymer and no obvious Bragg peaks due to any of the small molecules. In contrast, raP3HT is completely amorphous, while only the raP3HT:PDI blend shows obvious diffraction peaks of PDI. The largely vertical Bragg rods of PDI indicate that its crystallites are highly oriented relative to the substrate.

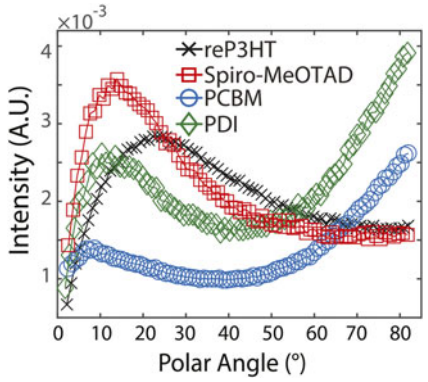


FIG. 3. Orientation distribution functions of the reP3HT lamellar (100) Bragg reflection as a function of the polar angle in neat reP3HT films as well as in blends with small molecules at the same monomer/small molecule mole ratio. The polar angle = 0° for the surface normal. PDI and PCBM blends show dual texture with a large face-on-oriented crystallite fraction, whereas Spiro-MeOTAD blends show primarily edge-on-oriented reP3HT crystallites.

in the lower panels of Fig. 2, which show a complete absence of P3HT Bragg peaks. PDI was the only small molecule that showed crystallite formation in raP3HT, which is consistent with its relatively planar core, leading to relatively strong π-stacking interactions. Interestingly, this suggests that in reP3HT blends, partial crystallization of the polymer may limit crystallization by the PDI. We found that changing the solvent from the rapidly evaporating chloroform to the lower vapor pressure chlorobenzene leads to the appearance of (isotropic) diffraction rings due to PDI as illustrated in Fig. S2. Thus, kinetic trapping of the initial film state may evidently lead to stunted PDI crystallization even after thermal annealing.

The GIXD images above clearly show that the distribution of reP3HT crystallite orientations relative to the substrate is a function of the small molecule chemical structure. To put this observation on a more quantitative footing, we have reduced 2D (100) reP3HT Bragg reflections to 1D crystallite orientation distribution functions (ODFs) by (i) first radially integrating the Bragg peak in polar coordinates over a small Q region centered about the peak, (ii) scaling the resulting intensity with a sin(polar angle) factor to account for the angular dependence of the number of crystallites contributing to diffraction at a given Q-space point,[13,39] and (iii) by normalizing the corrected intensity by its integral over the accessible polar angle range.

The ODF for pristine reP3HT films indicates lamellar crystallites with a preferred edge-on orientation between approximately 10–45° of the surface normal with a peak centered about 25°. As mentioned previously, both PCBM and PDI blends with reP3HT show bimodal texture; closer inspection of the ODFs for both molecules shows that the predominant P3HT crystallite orientation is face-on (π-stacking out-of-plane), with a minor fraction displaying an edge-on orientation. Interestingly, the ODF for the reP3HT:Spiro-MeOTAD blend indicates that P3HT crystallites in this blend are not only primarily edge-on-oriented, in contrast to the other small molecules, but that they are *more highly* edge-on-oriented than neat, thermally annealed reP3HT films. We can

https://doi.org/10.1557/jmr.2016.490 Published online by Cambridge University Press

operationally define the ratio of face-on- to edge-on-oriented crystallite populations as the ratio of ODF integrals from ~0° to 45 and 45° to ~90°. This calculation yields ratios of 0.52, 0.65, 1.04, and 1.23 for reP3HT:Spiro-MeOTAD, neat reP3HT, reP3HT:PDI, and reP3HT:PCBM, respectively.

B. Nanometer-scale morphology

We have used GISAXS link the Å-scale microstructure of our blend films with its nanometer-scale morphology responsible for long-distance charge transport through the interpenetrating polymer/molecule network.[40–43] Fig. 4 shows in-plane line cuts obtained from 2D GISAXS images near the image horizon. The monotonically decreasing GISAXS curve for the reP3HT:PCBM blend [Fig. 4(a)] shows two shoulders (plateau-like regions) at Q_{xy} ~0.03 Å^{-1} and Q_{xy} ~0.08 Å^{-1}, corresponding to two distinct characteristic length scales of roughly 20 and 8 nm, respectively. We interpret these features as arising due to the presence of a hierarchical blend network mesostructure, as no such features exist for pure reP3HT films. The 20 nm feature is possibly related to phase-separated P3HT crystallites—a size scale that has previously been observed for reP3HT blends using AFM.[44–46] The second length scale of ~8 nm is consistent with small, largely disordered PCBM clusters, which give rise to the broad scattering ring at wide angles at ~1.4 Å^{-1} [Fig. 2(a)]. We note in passing that, though tempting, using the Guinier approximation[47] to calculate effective radii of gyration from shoulder-like features in SAXS curves is problematic for thin blend films due to the expected importance of interparticle scattered wave interference.[48]

In stark contrast, reP3HT:PDI films give rise to a featureless GISAXS curve in the accessible Q range, suggesting two possible explanations: The PDI is fully miscible in the polymer matrix and forms no phase-separated aggregates on these length scales, or PDI aggregates are large enough so as to fall outside the limits of detection. For reP3HT:Spiro-MeOTAD blends, the GISAXS profile is similarly featureless with no obvious characteristics of phase separation over this length scale range.

Figure 4(b) shows GISAXS curves for raP3HT blend films. raP3HT:PCBM and raP3HT:PDI display featureless monotonic curves with no well-defined length scales of phase separation. Though similar to reP3HT:PDI blends, for PCBM this represents a drastic change in the microstructure relative to its morphology in the reP3HT matrix. This is not altogether surprising. Early work on organic solar cell performance based on conjugated polymer:PCBM blends showed that for semicrystalline reP3HT, the polymer:fullerene weight ratio that led to the maximum power conversion efficiency was close to 1:1.[49] However, for PCBM blends with amorphous MEH-PPV polymer, the optimal polymer:fullerene weight ratio was in the vicinity of 1:4, corresponding to an increased fullerene mole fraction relative to reP3HT blends.[50,51] Thus, if the electron current is largely limited by the microstructural state of the fullerene network, it may be hypothesized that the PCBM mole fraction leading to a near-optimal charge transport network within a conjugated polymer matrix depends on the polymer crystallite concentration. A detailed study of the microstructure evolution as a function of small molecule mole fraction is beyond the scope of this work.

Interestingly, the GISAXS curve for raP3HT:Spiro-MeOTAD blends shows a shoulder-like feature at Q_{xy} ~0.09 Å^{-1}, corresponding to an approximate length scale of 7 nm. This is similar to PCBM in reP3HT films. Thus, it appears that Spiro-MeOTAD—a nonspherical small molecule with 3D frontier molecular orbital extent—preferentially results in relatively well-defined length scale of polymer/molecule phase separation in the (thermally annealed) amorphous polymer host. This behavior is diametrically opposed to what we observed in P3HT blends with PCBM—the quintessential quasispherical small molecule. However, in both cases the small molecule gave rise to no obvious Bragg reflections in either polymer host; this differs qualitatively in raP3HT blends for PDI with its 2D molecular orbital extent.

To gain a better understanding of the difference in small molecule behavior as a function of polymer chain microstructure, we have used GIXD and GISAXS to interrogate blends of the three small molecules with a different amorphous polymer host. For this purpose,

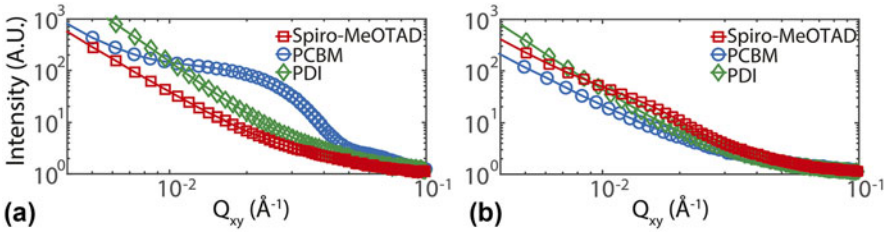


FIG. 4. Horizontal 1D line cuts of GISAXS patterns taken near the image horizon for (a) reP3HT and (b) raP3HT blends with different small molecules. Only reP3HT:PCBM and raP3HT:Spiro-MeOTAD blends show the appearance of shoulder-like features in this Q range, which are associated with formation of a characteristic length scale of polymer/small molecule phase separation on the nanometer scale. This feature is substantially more pronounced in the reP3HT:PCBM blend.

https://doi.org/10.1557/jmr.2016.490 Published online by Cambridge University Press

we have used poly(isobutylmethacrylate) (PIB), which has a molecular weight that is comparable to P3HT but a chemical structure that differs qualitatively from P3HT. The chemical structure of PIB is shown as an inset in Fig. 5, which displays GISAXS curves for both as-cast and thermally annealed PIB:molecule blends. We note that, although both polymers are amorphous, we expect that the difference in monomer chemical structure of PIB and raP3HT would lead to different inter-monomer (and possibly monomer-small molecule) interactions for the two polymers. However, a systematic investigation of blend microstructure as a function of polymer interaction parameters is beyond the scope of this work.

Figures 5(a) and 5(c) show that, similar to its behavior in raP3HT blends, PDI forms oriented crystallites and gives rise to a largely featureless scattering curves in both its as-cast and annealed states over the Q range accessible with GISAXS. The situation is entirely different for both PCBM and Spiro-MeOTAD. In PIB:PCBM films, the GISAXS curve for the as-cast film shows a shoulder-like feature at $Q \sim 0.02$ Å^{-1}, corresponding to a characteristic phase segregation length scale of roughly 30 nm. This feature partially disappears upon thermal annealing. In PIB:Spiro-MeOTAD blends, we observe precisely the oppositely behavior. Namely, the as-cast film gives rise to a featureless GISAXS profile, but upon thermal annealing a shoulder at $Q \sim 0.01$ Å^{-1} ($d \sim 60$ nm) becomes prominent. Thus, both molecules with little propensity for crystallization within the polymer matrix lead to phase separation on a length scale of the same order as common exciton diffusion lengths. However, for one molecule this corresponds to a kinetically frozen state (PCBM), whereas for the other (Spiro-MeOTAD), this state is located substantially closer in free energy to thermodynamic equilibrium.

The differences primarily between the morphology of polymer blends with PCBM and Spiro-OMeTAD—the two small molecules with a 3D molecular orbital extent—are intriguing yet puzzling. In particular, although Spiro-MeOTAD has demonstrated the ability to phase-segregate on the 10 s of nanometers length scale upon thermal annealing, GISAXS data implies that it does so only in amorphous polymer matrices. In an attempt to better understand these observations and to improve the comparison across the small molecule series, we have performed resonant elastic X-ray scattering (REXS) measurements in the vicinity of the carbon K-edge.[52–54] At these energies, this technique is sometimes referred to as resonant soft X-ray scattering.[55–58] Because atomic scattering factors become complex in the vicinity of an absorption edge, the scattering contrast can be tuned (and enhanced) by tuning the X-ray energy across the transition threshold. This technique not only allows us to extend our scattering measurements to lower Q and thus larger length scales, but we can also compare scattering off- and on-resonance (in the near-edge 1 s → π* transition region) to potentially

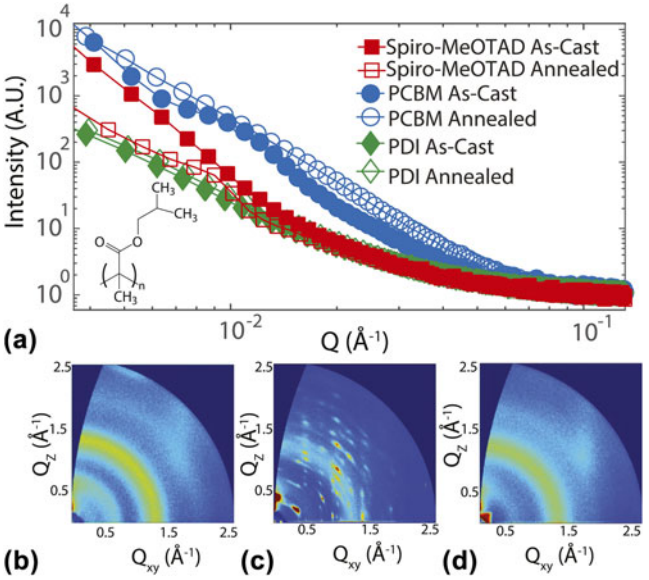


FIG. 5. (a) GISAXS curves for as-cast and thermally annealed blends of poly(isobutylmethacrylate) (PIB) with different small molecules. The chemical structure of PIB is shown as an inset. Upon annealing, only the PIB:Spiro-MeOTAD shows the appearance of a well-defined shoulder. A similar feature is evident in as-cast PIB:PCBM blends but largely disappears upon annealing. The lower panels show GIXD patterns for annealed blends of PIB with (b) PCBM, (c) PDI, (d) Spiro-MeOTAD. The images show that, similar to raP3HT blends, PDI forms highly oriented crystallites within the polymer matrix.

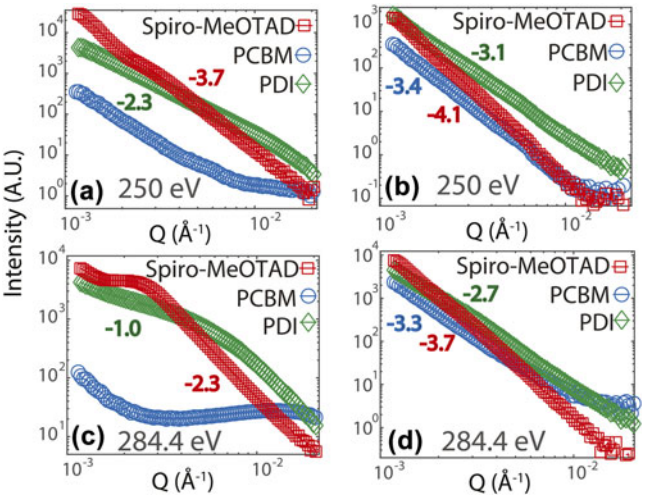


FIG. 6. REXS curves collected in the vicinity of the carbon K-edge for reP3HT (a, c) and raP3HT (b, d) blends with the three small molecules. The top panels (a, b) correspond to scattering of 250 eV photons, which is well below the carbon K-edge absorption onset. The bottom panels (c, d) correspond to 284.4 eV photons, which is just above the absorption onset. Higher energies did not give rise to curves that differed qualitatively from those collected at 284.4 eV. reP3HT:Spiro-MeOTAD and reP3HT:PDI show signatures of clustering on the 100 nm scale, which is too large for efficient charge generation. All raP3HT blends give rise to relatively featureless curves, though with power law exponents (over certain Q windows) that differ significantly among the three small molecules. The fitted power law exponents are shown next to the curves.

https://doi.org/10.1557/jmr.2016.490 Published online by Cambridge University Press

gain additional insight into the nature of the scattering inhomogeneities due to energy-dependent scattering contrast differences. X-ray absorption spectra of the probed molecules is shown in Fig. S6.

Figure 6 shows REXS curves of reP3HT (a, c) and raP3HT (b, d) blend films. reP3HT:PCBM films both off- and on-resonance look qualitatively similar: The scattered intensity appears to plateau at $Q \sim 0.01$ Å^{-1}, which is very consistent with the position of the well-defined shoulder observed with GISAXS in the same blends. Further support for this is shown in Fig. S5 of the Supplementary Material, which shows that the on-resonance REXS curve for this blend is qualitatively similar to GISAXS data. For reP3HT:PDI blends, the off-resonant scattering intensity I is well represented by power law scaling over the measured Q range, that is, $I \propto Q^p$, where p is negative. On resonance, however, the reP3HT:PDI curve displays a relatively well-defined shoulder roughly corresponding to a 90 nm length scale. This implies that the contribution of the so-called pure resonant scattering function to the total intensity becomes substantial, thus modifying the effective contrast responsible for low-Q scattering. This must be due to reasonably strong contrast between the π-electron density (when probing near the absorption edge) and the surrounding matrix. We may expect this to be the case for highly segregated PDI clusters.

Interestingly, off-resonant REXS curves of reP3HT:Spiro-MeOTAD films contain a shoulder at a fairly low Q of ~ 0.003 Å^{-1}, which corresponds to approximately 210 nm. The location of this feature moves slightly to lower Q when the X-ray energy is tuned on resonance while at the same time becoming more pronounced. Thus, together with GISAXS data, our results show that reP3HT:Spiro-MeOTAD blends are devoid of well-defined morphological features on the 10 nm scale but contain large scattering inhomogeneities well in excess of expected exciton diffusion lengths. We note that at larger Q, the intensity is well represented by a power law; in the figure we have indicated the values of p obtained from fitting the intensity to such a model.

REXS curves for raP3HT blends with all three small molecules display significant differences in slope among the different molecules but no obvious shoulder-like features commonly associated with relatively well-defined length scales of phase separation. Such behavior may result from fractal-like morphologies, though we are unable to verify this at the moment. However, as mentioned above, raP3HT:Spiro-MeOTAD does show evidence for clustering on the 10 nm scale, which stands in contrast to both PCBM and PDI in raP3HT.

III. DISCUSSION

We begin by discussing the implications of Å-scale structural measurements. The GIXD images show that the polymer crystallite ODF differs qualitatively for different small molecules. Compared to the neat reP3HT film, the small molecule chemical structure effectively dictates whether polymer crystallites are oriented edge-on, corresponding to poor vertical charge transport through the crystalline regions, versus face-on, which is nominally desired for optimal vertical hole mobilities.[59] Thus, it can generally be expected that the thickness-averaged intermolecular hole transfer rate through the P3HT network is generally a sensitive function of the small molecule chemical structure. However, the data do not make clear *why* PDI and PCBM tend to result in a predominantly face-on oriented crystallite distribution and why Spiro-MeOTAD in fact improves the propensity for P3HT crystallites to orient edge-on. The possibility of modifying the small molecule chemical structure to tune the polymer ODF is intriguing, though it may be important to appreciate that the nanometer-scale morphology may in principle depend on the ODF. Nevertheless, though both PDI and PCBM resulted in a primarily face-on reP3HT ODF, their mesoscale blend morphology differed drastically.

The morphology of PCBM blends stood out among the small molecule series as the only one that in reP3HT—a semicrystalline polymer matrix—showed a well-defined feature of phase segregation on a length scale that is compatible with expected polymer exciton diffusion lengths. The propensity to phase segregate on comparable length scales for PCBM was lost in the amorphous raP3HT. The latest understanding of semicrystalline reP3HT films paints a picture of nanocrystallites connected to one another via tie chains.[36,60–62] Space between crystallites is considered largely amorphous; PCBM boasts a relatively large solid state solubility in these regions.[36,60] We hypothesize that P3HT crystallites confine fullerene molecules to the inter-crystallite space, where their spherical shape and fairly small size, as judged by the solvent-excluded volume (735 Å^3, see Supplementary Material), lead to highly efficient packing and well-defined interpenetrating network formation. In entirely amorphous raP3HT, there is little confinement due to relatively dense polymer regions, and PCBM disperses evenly throughout. Such a situation would give rise to a fairly featureless scattering curve at low Q, which is what we observed.

In contrast to PCBM, due its planar conjugated core, PDI has a propensity to form large aggregates and crystallites upon thermal annealing. This leads to little evidence for phase separation on a length scale relevant for exciton diffusion, independent of the polymer chain microstructure. This is consistent with the substantially decreased photovoltaic power conversion efficiencies for PDI blends relative to PCBM.[63–65] Further, the solvent-excluded volume for PDI is roughly twice as large as that of PCBM (1418 Å^3), leading to less efficient packing

https://doi.org/10.1557/jmr.2016.490 Published online by Cambridge University Press

compared to PCBM. In addition to the fact that for such a highly anisotropic molecule, inter-PDI electron transfer is a sensitive function of the relative molecular orientation,[27,29] the strong anisotropic π-stacking interactions lead to large-scale aggregate or crystallite growth that is incompatible with efficient exciton harvesting.

The behavior of Spiro-MeOTAD appears to be more complex and at the moment quite puzzling. First, it is curious that this is the one small molecule, whose reP3HT blends resulted in a population of face-on-oriented polymer crystallites that was smaller than the neat polymer film itself. Second, Spiro-MeOTAD showed no evidence for phase-segregated mesoscale network formation in reP3HT. It is possible that Spiro-MeOTAD is simply too large (solvent-excluded volume = 1463 Å^3) to form a molecular network the penetrates through the amorphous P3HT regions connecting polymer crystallites, or that its molecular packing is poor relative to the quasispherical PCBM. REXS measurements showed that the film does show a characteristic length scale that is of order 100 nm, too large to form an interpenetrating network with a significant internal quantum efficiency. This does not appear to hold for raP3HT and PIB blends with Spiro-MeOTAD, which show signatures of phase segregation on the 10 nm scale, though neither was as pronounced as reP3HT:PCBM. We hypothesize that perhaps removal of the physical constraints imposed by polymer crystallites lead to a somewhat enhanced ability to form relatively nanoscale small clusters, though additional experiments are necessary to fully understand this behavior. This suggests that for relatively large non-spherical small molecules, a largely amorphous polymer matrix may be desired. Figure 7 shows cartoons of local and nanoscale network microstructure in semicrystalline reP3HT as a function of small molecule that emerges from our results. Future work will focus on elucidating the influence of peripheral functional groups of a Spiro derivative series on the polymer crystallite ODF and the mesoscale morphology.

The data presented above make it unambiguously clear that, for a given set of processing parameters, the chemical structure of the small molecule *along with* the polymer chain microstructure can drastically alter the interpenetrating polymer/molecule network that underpins charge transport in such blend films. Our results make clear that the polymer chain microstructure couples to the small molecule structure in directing the end-state morphology. Thus, it makes little sense to take a nominally high-performance conjugated polymer optimized for, say, PCBM and to expect that the same polymer will form a comparable charge transport network when a different electron acceptor is used. Conversely, this suggests that polymers discarded due to nominally poor performance in PCBM blends may well reach their full potential when combined with a small-molecule electron acceptor with an entirely different molecular geometry.

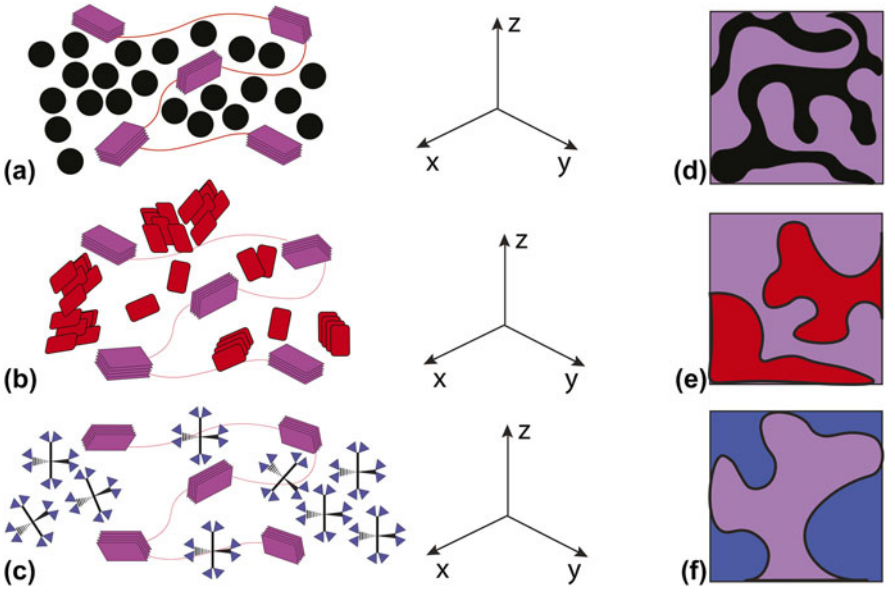


FIG. 7. Cartoons of local polymer/molecule blend microstructure in reP3HT blends containing (a) PCBM, (b) PDI, and (c) Spiro-MeOTAD. The coordinate system shown on the right corresponds to the sample reference frame, where the z axis is the direction normal to the film surface, and the xy plan corresponds to the plane of the substrate. Cartoons of interpenetrating nanoscale network morphology for each small molecule are shown in (d), (e) and (f) for PCBM, PDI and Spiro-MeOTAD blends, respectively. Purple corresponds to the polymer phase. The data indicate that PCBM blends result in nanoscale networks with PCBM molecules infiltrating amorphous regions between reP3HT crystallites. In contrast, PDI and Spiro-MeOTAD blends lead to large clusters well in excess of the exciton diffusion length. The exciton diffusion length is comparable to the mean separation between fullerene channels (black) in (d). These cartoons necessarily correspond to a significant oversimplification of the blend microstructural hierarchy.

https://doi.org/10.1557/jmr.2016.490 Published online by Cambridge University Press

One conclusion is that the current inability to appreciate the morphological implications of component chemical structures at the outset may lead to substantial synthetic and processing efforts that ultimately fail to explore the relevant chemical structure-dependent parameter space. For the OPV field to successfully move beyond the fullerene electron acceptor in a systematic fashion, elucidating such a link will likely prove pivotal. This manuscript was an attempt to move in such a direction, though we have barely scratched the surface of this extremely complex many-body problem. However, our work shows that we can make progress through careful examination of the microstructure as a function of chemical structure simultaneously across multiple length scales.

IV. CONCLUSIONS

The motivation for this work was to begin to systematically understand how the chemical structure of the small molecule influences the local and meso-scale microstructure in the blend polymer/molecule film. Though there is a near-infinite synthetic space to explore, we focused on a few small molecules, whose geometry and molecular orbital extent different qualitatively. We found that the different small molecules resulted in different long-range order of the semicrystalline polymer matrix. Further, we showed that the nanometer-scale morphology is a sensitive function of the small molecule chemical structure, and that the ability of a molecule to form clusters associated with desirable phase-separated networks is coupled to the polymer chain microstructure. These results highlight the need for a continued in-depth exploration of the microstructural hierarchy in polymer/small molecules blends for different geometric and electronic molecular motifs.

ACKNOWLEDGMENTS

GIXD measurements were performed at the Stanford Synchrotron Radiation Laboratory, a national user facility operated by the U.S. Department of Energy, Office of Basic Energy Sciences; the authors would like to acknowledge Tim Dunn for his beamline support. We thank Stefan Mannsfeld (Dresden University of Technology, Germany) for providing software used to process GIXD images. GISAXS and REXS data were acquired at the Advanced Light Source at the Lawrence Berkeley National Laboratory also operated by the U.S. Department of Energy, Basic Sciences Division; the authors acknowledge Dr. Cheng Wang and Dr. Mike Brady for their beamline training and support. GISAXS data were calibrated and reduced using a MATLAB program written by Victoria Savikhin (Stanford University). Solvent-excluded volume and surface area calculations were performed by Cameron Pye (University of California, Santa Cruz) using Biovia's Discovery Studio.

REFERENCES

1. N.S. Sariciftci, L. Smilowitz, D. Braun, G. Srdanov, V. Srdanov, F. Wudl, and A.J. Heeger: Observation of a photoinduced electron transfer from a conducting polymer (MEHPPV) onto C_{60}. *Synth. Met.* **56**(2), 3125 (1993).
2. C.Y. Yang and A.J. Heeger: Morphology of composites of semiconducting polymers mixed with C_{60}. *Synth. Met.* **83**(2), 85 (1996).
3. G. Dennler, M.C. Scharber, and C.J. Brabec: Polymer-fullerene bulk-heterojunction solar cells. *Adv. Mater.* **21**(13), 1323 (2009).
4. Y. Huang, E.J. Kramer, A.J. Heeger, and G.C. Bazan: Bulk heterojunction solar cells: morphology and performance relationships. *Chem. Rev.* **114**(14), 7006 (2014).
5. S.H. Park, A. Roy, S. Beaupre, S. Cho, N. Coates, J.S. Moon, D. Moses, M. Leclerc, K. Lee, and A.J. Heeger: Bulk heterojunction solar cells with internal quantum efficiency approaching 100%. *Nat. Photonics* **3**(5), 297 (2009).
6. K. Vandewal, S. Himmelberger, and A. Salleo: Structural factors that affect the performance of organic bulk heterojunction solar cells. *Macromolecules* **46**(16), 6379 (2013).
7. K. Vandewal, K. Tvingstedt, and O. Inganäs: Charge transfer states in organic donor–acceptor sol cells. *Semicond. Semimetals* **85**, 261 (2011).
8. S.D. Dimitrov and J.R. Durrant: Materials design considerations for charge generation in organic solar cells. *Chem. Mater.* **26**(1), 616 (2014).
9. J.T. Rogers, K. Schmidt, M.F. Toney, E.J. Kramer, and G.C. Bazan: Structural order in bulk heterojunction films prepared with solvent additives. *Adv. Mater.* **23**(20), 2284 (2011).
10. A.L. Ayzner, D.D. Wanger, C.J. Tassone, S.H. Tolbert, and B.J. Schwartz: Room to improve conjugated polymer-based solar cells: Understanding how thermal annealing affects the fullerene component of a bulk heterojunction photovoltaic device. *J. Phys. Chem. C* **112**(48), 18711 (2008).
11. E. Verploegen, R. Mondal, C.J. Bettinger, S. Sok, M.F. Toney, and Z. Bao: Effects of thermal annealing upon the morphology of polymer–fullerene blends. *Adv. Funct. Mater.* **20**(20), 3519 (2010).
12. L. Zheng, J. Liu, Y. Ding, and Y. Han: Morphology evolution and structural transformation of solution-processed methanofullerene thin film under thermal annealing. *J. Phys. Chem. B* **115**(25), 8071 (2011).
13. D.M. DeLongchamp, R.J. Kline, D.A. Fischer, L.J. Richter, and M.F. Toney: Molecular characterization of organic electronic films. *Adv. Mater.* **23**(3), 319 (2011).
14. D. Kurrle and J. Pflaum: Exciton diffusion length in the organic semiconductor diindenoperylene. *Appl. Phys. Lett.* **92**(13), 133306 (2008).
15. J.D.A. Lin, O.V. Mikhnenko, J. Chen, Z. Masri, A. Ruseckas, A. Mikhailovsky, R.P. Raab, J. Liu, P.W.M. Blom, M.A. Loi, C.J. García-Cervera, I.D.W. Samuel, and T-Q. Nguyen: Systematic study of exciton diffusion length in organic semiconductors by six experimental methods. *Mater. Horiz.* **1**(2), 280 (2014).
16. W.A. Luhman and R.J. Holmes: Investigation of energy transfer in organic photovoltaic cells and impact on exciton diffusion length measurements. *Adv. Funct. Mater.* **21**(4), 764 (2011).
17. R.R. Lunt, J.B. Benziger, and S.R. Forrest: Relationship between crystalline order and exciton diffusion length in molecular organic semiconductors. *Adv. Mater.* **22**(11), 1233 (2010).
18. R.R. Lunt, N.C. Giebink, A.A. Belak, J.B. Benziger, and S.R. Forrest: Exciton diffusion lengths of organic semiconductor thin films measured by spectrally resolved photoluminescence quenching. *J. Appl. Phys.* **105**(5), 053711 (2009).

https://doi.org/10.1557/jmr.2016.490 Published online by Cambridge University Press

19. S-B. Rim, R.F. Fink, J.C. Schöneboom, P. Erk, and P. Peumans: Effect of molecular packing on the exciton diffusion length in organic solar cells. *Appl. Phys. Lett.* **91**(17), 173504 (2007).
20. J. You, L. Dou, K. Yoshimura, T. Kato, K. Ohya, T. Moriarty, K. Emery, C.C. Chen, J. Gao, G. Li, and Y. Yang: A polymer tandem solar cell with 10.6% power conversion efficiency. *Nat. Commun.* **4**, 1446 (2013).
21. L. Pandey, C. Risko, J.E. Norton, and J-L. Brédas: Donor–acceptor copolymers of relevance for organic photovoltaics: A theoretical investigation of the impact of chemical structure modifications on the electronic and optical properties. *Macromolecules* **45**(16), 6405 (2012).
22. D.H. Kim, A.L. Ayzner, A.L. Appleton, K. Schmidt, J. Mei, M.F. Toney, and Z. Bao: Comparison of the photovoltaic characteristics and nanostructure of fullerenes blended with conjugated polymers with siloxane-terminated and branched aliphatic side chains. *Chem. Mater.* **25**(3), 431 (2013).
23. T. Liu and A. Troisi: What makes fullerene acceptors special as electron acceptors in organic solar cells and how to replace them. *Adv. Mater.* **25**(7), 1038 (2013).
24. G. Sauvé and R. Fernando: Beyond fullerenes: Designing alternative molecular electron acceptors for solution-processable bulk heterojunction organic photovoltaics. *J. Phys. Chem. Lett.* **6**(18), 3770 (2015).
25. G. Orlandi and F. Negri: Electronic states and transitions in C_{60} and C70 fullerenes. *Photochem. Photobiol. Sci.* **1**(5), 289 (2002).
26. R. Shivanna, S. Shoaee, S. Dimitrov, S.K. Kandappa, S. Rajaram, J.R. Durrant, and K.S. Narayan: Charge generation and transport in efficient organic bulk heterojunction solar cells with a perylene acceptor. *Energy Environ. Sci.* **7**(1), 435 (2014).
27. D. Beljonne, J.r.m. Cornil, L. Muccioli, C. Zannoni, J-L. Brédas, and F.d.r. Castet: Electronic processes at organic–organic interfaces: Insight from modeling and implications for opto-electronic devices†. *Chem. Mater.* **23**(3), 591 (2011).
28. B.P. Rand, D. Cheyns, K. Vasseur, N.C. Giebink, S. Mothy, Y. Yi, V. Coropceanu, D. Beljonne, J. Cornil, J-L. Brédas, and J. Genoe: The impact of molecular orientation on the photovoltaic properties of a phthalocyanine/fullerene heterojunction. *Adv. Funct. Mater.* **22**(14), 2987 (2012).
29. A.L. Ayzner, D. Nordlund, D-H. Kim, Z. Bao, and M.F. Toney: Ultrafast electron transfer at organic semiconductor interfaces: Importance of molecular orientation. *J. Phys. Chem. Lett.* **6**(1), 6 (2015).
30. S. Wang, S. Fabiano, S. Himmelberger, S. Puzinas, X. Crispin, A. Salleo, and M. Berggren: Experimental evidence that short-range intermolecular aggregation is sufficient for efficient charge transport in conjugated polymers. *Proc. Natl. Acad. Sci. U. S. A.* **112**(34), 10599 (2015).
31. J. Als-Nielsen, D. Jacquemain, K. Kjaer, F. Leveiller, M. Lahav, and L. Leiserowitz: Principles and applications of grazing incidence X-ray and neutron scattering from ordered molecular monolayers at the air–water interface. *Phys. Rep.* **246**(5), 251 (1994).
32. A.C. Cruickshank, C.J. Dotzler, S. Din, S. Heutz, M.F. Toney, and M.P. Ryan: The crystalline structure of copper phthalocyanine films on ZnO(1100). *J. Am. Chem. Soc.* **134**(35), 14302 (2012).
33. S.E. Fritz, S.M. Martin, C.D. Frisbie, M.D. Ward, and M.F. Toney: Structural characterization of a pentacene monolayer on an amorphous SiO_2 substrate with grazing incidence x-ray diffraction. *J. Am. Chem. Soc.* **126**(13), 4084 (2004).
34. M. Ofuji, K. Inaba, K. Omote, H. Hoshi, Y. Takanishi, K. Ishikawa, and H. Takezoe: Grazing incidence in-plane X-ray diffraction study on oriented copper phthalocyanine thin films. *Jpn. J. Appl. Phys., Part 1* **41**(8), 5467 (2002).
35. G.H. Vineyard: Grazing-incidence diffraction and the distorted-wave approximation for the study of surfaces. *Phys. Rev. B: Condens. Matter Mater. Phys.* **26**(8), 4146 (1982).
36. N.D. Treat, M.A. Brady, G. Smith, M.F. Toney, E.J. Kramer, C.J. Hawker, and M.L. Chabinyc: Interdiffusion of PCBM and P3HT reveals miscibility in a photovoltaically active blend. *Adv. Energy Mater.* **1**(1), 82 (2011).
37. D. Gargi, R.J. Kline, D.M. DeLongchamp, D.A. Fischer, M.F. Toney, and B.T. O'Connor: Charge transport in highly face-on poly(3-hexylthiophene) films. *J. Phys. Chem. C* **117**(34), 17421 (2013).
38. B. O'Connor, R.J. Kline, B.R. Conrad, L.J. Richter, D. Gundlach, M.F. Toney, and D.M. DeLongchamp: Anisotropic structure and charge transport in highly strain-aligned regioregular poly(3-hexylthiophene). *Adv. Funct. Mater.* **21**(19), 3697 (2011).
39. J.L. Baker, L.H. Jimison, S. Mannsfeld, S. Volkman, S. Yin, V. Subramanian, A. Salleo, A.P. Alivisatos, and M.F. Toney: Quantification of thin film crystallographic orientation using x-ray diffraction with an area detector. *Langmuir* **26**(11), 9146 (2010).
40. S. Guo, M.A. Ruderer, M. Rawolle, V. Korstgens, C. Birkenstock, J. Perlich, and P. Muller-Buschbaum: Evolution of lateral structures during the functional stack build-up of P3HT:PCBM-based bulk heterojunction solar cells. *ACS Appl. Mater. Interfaces* **5**(17), 8581 (2013).
41. M. Rauscher, T. Salditt, and H. Spohn: Small-angle X-ray scattering under grazing incidence: The cross section in the distorted-wave Born approximation. *Phys. Rev. B: Condens. Matter Mater. Phys.* **52**(23), 16855 (1995).
42. G. Renaud, R. Lazzari, and F. Leroy: Probing surface and interface morphology with grazing incidence small angle X-ray scattering. *Surf. Sci. Rep.* **64**(8), 255 (2009).
43. G. Ungar, F. Liu, X.B. Zeng, B. Glettner, M. Prehm, R. Kieffer, and C. Tschierske: GISAXS in the study of supramolecular and hybrid liquid crystals. *J. Phys.: Conf. Ser.* **247**, 012032 (2010).
44. M. Dante, J. Peet, and T-Q. Nguyen: Nanoscale charge transport and internal structure of bulk heterojunction conjugated polymer/fullerene solar cells by scanning probe microscopy. *J. Phys. Chem. C* **112**(18), 7241 (2008).
45. C.J. Tassone, A.L. Ayzner, R.D. Kennedy, M. Halim, M. So, Y. Rubin, S.H. Tolbert, and B.J. Schwartz: Using pentaarylfullerenes to understand network formation in conjugated polymer-based bulk-heterojunction solar cells. *J. Phys. Chem. C* **115**(45), 22563 (2011).
46. A.L. Ayzner, C.J. Tassone, S.H. Tolbert, and B.J. Schwartz: Reappraising the need for bulk heterojunctions in polymer–fullerene photovoltaics: The role of carrier transport in all-solution-processed P3HT/PCBM bilayer solar cells. *J. Phys. Chem. C* **113**(46), 20050 (2009).
47. A. Guinier: *X-ray Diffraction: In Crystals, Imperfect Crystals, and Amorphous Bodies* (Dover Publications, Mineola, 2013).
48. B. Weyerich, J. Brunner-Popela, and O. Glatter: Small-angle scattering of interacting particles. II. Generalized indirect Fourier transformation under consideration of the effective structure factor for polydisperse systems. *J. Appl. Crystallogr.* **32**(2), 197 (1999).
49. Y. Kim, S.A. Choulis, J. Nelson, D.D.C. Bradley, S. Cook, and J.R. Durrant: Composition and annealing effects in polythiophene/fullerene solar cells. *J. Mater. Sci.* **40**(6), 1371 (2005).
50. H. Hoppe and N.S. Sariciftci: Morphology of polymer/fullerene bulk heterojunction solar cells. *J. Mater. Chem.* **16**(1), 45 (2006).
51. V. Shrotriya, G. Li, Y. Yao, T. Moriarty, K. Emery, and Y. Yang: Accurate measurement and characterization of organic solar cells. *Adv. Funct. Mater.* **16**(15), 2016 (2006).
52. J. Fink, E. Schierle, E. Weschke, and J. Geck: Resonant elastic soft X-ray scattering. *Rep. Prog. Phys.* **76**(5), 056502 (2013).
53. S. Grenier and Y. Joly: Basics of resonant elastic X-ray scattering theory. *J. Phys.: Conf. Ser.* **519**, 012001 (2014).

https://doi.org/10.1557/jmr.2016.490 Published online by Cambridge University Press

54. C. Vettier: Resonant elastic X-ray scattering: Where from? Where to?. *Eur. Phys. J.: Spec. Top.* **208**(1), 3 (2012).
55. F. Liu, M.A. Brady, and C. Wang: Resonant soft X-ray scattering for polymer materials. *Eur. Polym. J.* **81**, 555 (2016).
56. C. Wang, D.H. Lee, A. Hexemer, M.I. Kim, W. Zhao, H. Hasegawa, H. Ade, and T.P. Russell: Defining the nanostructured morphology of triblock copolymers using resonant soft X-ray scattering. *Nano Lett.* **11**(9), 3906 (2011).
57. T. Araki, H. Ade, J.M. Stubbs, D.C. Sundberg, G.E. Mitchell, J.B. Kortright, and A.L.D. Kilcoyne: Resonant soft X-ray scattering from structured polymer nanoparticles. *Appl. Phys. Lett.* **89**(12), 124106 (2006).
58. B.A. Collins, J.E. Cochran, H. Yan, E. Gann, C. Hub, R. Fink, C. Wang, T. Schuettfort, C.R. McNeill, M.L. Chabinyc, and H. Ade: Polarized X-ray scattering reveals non-crystalline orientational ordering in organic films. *Nat. Mater.* **11**(6), 536 (2012).
59. J. Rivnay, M.F. Toney, Y. Zheng, I.V. Kauvar, Z. Chen, V. Wagner, A. Facchetti, and A. Salleo: Unconventional face-on texture and exceptional in-plane order of a high mobility n-type polymer. *Adv. Mater.* **22**(39), 4359 (2010).
60. A.L. Ayzner, S.C. Doan, B. Tremolet de Villers, and B.J. Schwartz: Ultrafast studies of exciton migration and polaron formation in sequentially solution-processed conjugated polymer/fullerene quasi-bilayer photovoltaics. *J. Phys. Chem. Lett.* **3**(16), 2281 (2012).
61. H.W. Ro, B. Akgun, B.T. O'Connor, M. Hammond, R.J. Kline, C.R. Snyder, S.K. Satija, A.L. Ayzner, M.F. Toney, C.L. Soles, and D.M. DeLongchamp: Poly(3-hexylthiophene) and [6,6]-phenyl-C61-butyric acid methyl ester mixing in organic solar cells. *Macromolecules* **45**(16), 6587 (2012).
62. D. Chen, F. Liu, C. Wang, A. Nakahara, and T.P. Russell: Bulk heterojunction photovoltaic active layers via bilayer interdiffusion. *Nano Lett.* **11**(5), 2071 (2011).
63. Q. Yan, Y. Zhou, Y-Q. Zheng, J. Pei, and D. Zhao: Towards rational design of organic electron acceptors for photovoltaics: A study based on perylenediimide derivatives. *Chem. Sci.* **4**(12), 4389 (2013).
64. A. Sharenko, C.M. Proctor, T.S. van der Poll, Z.B. Henson, T-Q. Nguyen, and G.C. Bazan: A high-performing solution-processed small molecule:perylene diimide bulk heterojunction solar cell. *Adv. Mater.* **25**(32), 4403 (2013).
65. V. Kamm, G. Battagliarin, I.A. Howard, W. Pisula, A. Mavrinskiy, C. Li, K. Müllen, and F. Laquai: Polythiophene:perylene diimide solar cells—The impact of alkyl-substitution on the photovoltaic performance. *Adv. Energy Mater.* **1**(2), 297 (2011).

Supplementary Material

To view supplementary material for this article, please visit https://doi.org/10.1557/jmr.2016.490.

https://doi.org/10.1557/jmr.2016.490 Published online by Cambridge University Press